Two-atomic-layered optoelectronic device enabled by charge separation on graphene/semiconductor interface

Qirong Yang, (iD) Jianxin Guan, Jingwen Deng, et al.

COLLECTIONS

Paper published as part of the special topic on Transport of Charge and Energy in Low-Dimensional Materials

View Online   Export Citation   CrossMark

ARTICLES YOU MAY BE INTERESTED IN

Two-atomic-layered optoelectronic device enabled by charge separation on graphene/semiconductor interface

View Online   Export Citation   CrossMark

Qirong Yang,[1] Jianxin Guan,[1] (iD) Jingwen Deng,[1] Zihan Xu,[2] Zhihao Yu,[1] (iD) and Junrong Zheng[1,a] (iD)

AFFILIATIONS

[1] College of Chemistry and Molecular Engineering, Beijing National Laboratory for Molecular Sciences, Peking University, Beijing 100871, China

[2] Shenzhen Sixcarbon Technology, Shenzhen 518106, China

Note: This paper is part of the JCP Special Topic on Transport of Charge and Energy in Low-Dimensional Materials.
[a] Author to whom correspondence should be addressed: junrong@pku.edu.cn and zhengjunrong@gmail.com

ABSTRACT

The Fermi level of graphene on different substrates usually changes significantly due to the interface difference between graphene and two-dimensional semiconductors. This feature opens many possibilities of manipulating optoelectronic devices by constructing graphene heterostructures through interface modification. Herein, we report the fabrication and optoelectronic response of an unconventional heterojunction device based on a graphene–MoSe$_2$ hybrid interface. Different from the traditional three or more layered structure where the semiconductor is sandwiched between two electrodes, this device contains only two atomic layers: the MoSe$_2$ layer serving as the photon absorber and the graphene layer functioning as the charge acceptor and both electrodes. This structure looks like short-circuited but shows an obvious photoelectric response, which is aided by electron transfers from MoSe$_2$ to graphene. The photocurrent generation is explored quantitatively with electronic dynamics of graphene aided with ultrafast measurements. The two-layered architecture simplifies the fabrication of atomic-thick optoelectronic devices, allowing the as-grown semiconductors to be directly used and eliminating the damage-prone transfer process.

Published under an exclusive license by AIP Publishing. https://doi.org/10.1063/5.0065110

I. INTRODUCTION

Atomic-thin optoelectronic devices based on two dimensional (2D) materials are promising candidates for the next generation of sensing, displaying, and solar energy utilizations.[1] An atomic-thin optoelectronic device is typically composed of a layer of 2D semiconductor sandwiched between two electrodes.[2–4] One of the electrodes is transparent or semi-transparent, e.g., graphene or ITO.[5–10] To fabricate such a device, the 2D semiconductor layer is peeled off from its as-grown substrate and transferred to the top of an electrode, except a few cases where the semiconductor can be directly grown on the electrode.[11] A typical 2D semiconductor single crystal is only of a few to tens of microns wide and one atomic layer thick, e.g., a CVD grown 2D MoSe$_2$ crystal.[12] The small dimension and the fragile nature of the semiconductor layer make the transfer process nontrivial. Both skills and great care are indispensable. Otherwise, the semiconductor layer can be easily

damaged, and the two electrodes can be short-circuited. It is, therefore, very desirable if the transfer of the semiconductor layer can be avoided and the as-grown sample on the substrate can be used directly. However, typical substrates for the growth of 2D semiconductors are silica or Si, the surface of which is a layer of SiO$_2$. They cannot function as electrodes. If the semiconductor layer is required to remain on the as-grown substrate, both the electrodes of the device must be on the same sides of the semiconductor layer, which seems to be impossible to be a functioning layout because the charges generated in the semiconductor layer seem not be able to properly separate and flow into the electrodes.

In principle, the difficulties discussed above can be addressed if the electrodes are graphene. Graphene has a high carrier mobility but relatively low light absorption,[13–16] promising as electrodes for atomic-thin optoelectronic devices. In perfect graphene, charge carriers are massless. When combined with other 2D materials to form

heterostructures, the Fermi level of graphene can be significantly modified, and its symmetry can be slightly broken,[17–21] leading to the effective mass change of charge carriers. In other words, within a large continuous graphene film, the portion stacked with another 2D material (photon absorber), e.g., TMD, would have electronic properties different from the remaining portion. If the charge separation between the photon absorber and graphene is sufficiently long, a device composed of only two atomic layers is feasible, where the portion of graphene stacked with the photon absorber functions as one electrode and the remaining portion acts as the other electrode, provided that the electric resistance of the external circuit is not significantly larger than that of graphene. In this work, we report such a two-layered heterojunction based on the graphene–$MoSe_2$ hybrid interface.

II. RESULTS AND DISCUSSION

A. Graphene/$MoSe_2$ heterostructure

The structure of a two-atomic-layered optoelectronic device is illustrated in Fig. 1(a). An atomic layer of single crystal $MoSe_2$ on the SiO_2/Si substrate is used as grown. A layer of graphene that is larger than $MoSe_2$ is placed on the top of $MoSe_2$. Two gold conducting layers about 120 nm thick are deposited on the top of the heterostructure and bare graphene, serving as connectors to the external circuit. The monolayer $MoSe_2$ is a direct bandgap semiconductor, and its interband optical absorption is anomalously strong.[22] The monolayer graphene has a very high carrier mobility, which can result in a rapid Fermi–Dirac electronic redistribution when optical excitations generate free carriers.[23] When the heterostructure shines with light, the charge separation on the heterojunction changes the Fermi level of graphene, a potential difference is generated between the $MoSe_2$ stacked portion and the rest of the graphene, and a photocurrent is produced and detected in the external circuit.

An optical image of the heterojunction is displayed in Fig. 1(b). The triangle is the monolayer of $MoSe_2$, on the top of which is a monolayer of p-doped graphene. The monolayer $MoSe_2$ and graphene are grown on a Si substrate with a 300 nm SiO_2 layer and an electro-polished copper foil by the chemical vapor deposition (CVD) method, respectively. The graphene is then transferred onto the $MoSe_2$ film by wet transfer technology.[24] The monolayer graphene is not visible in the optical image, but it can be easily observed with Raman spectroscopic measurements. Figure 1(c) displays the Raman spectra of monolayer $MoSe_2$, graphene, and the
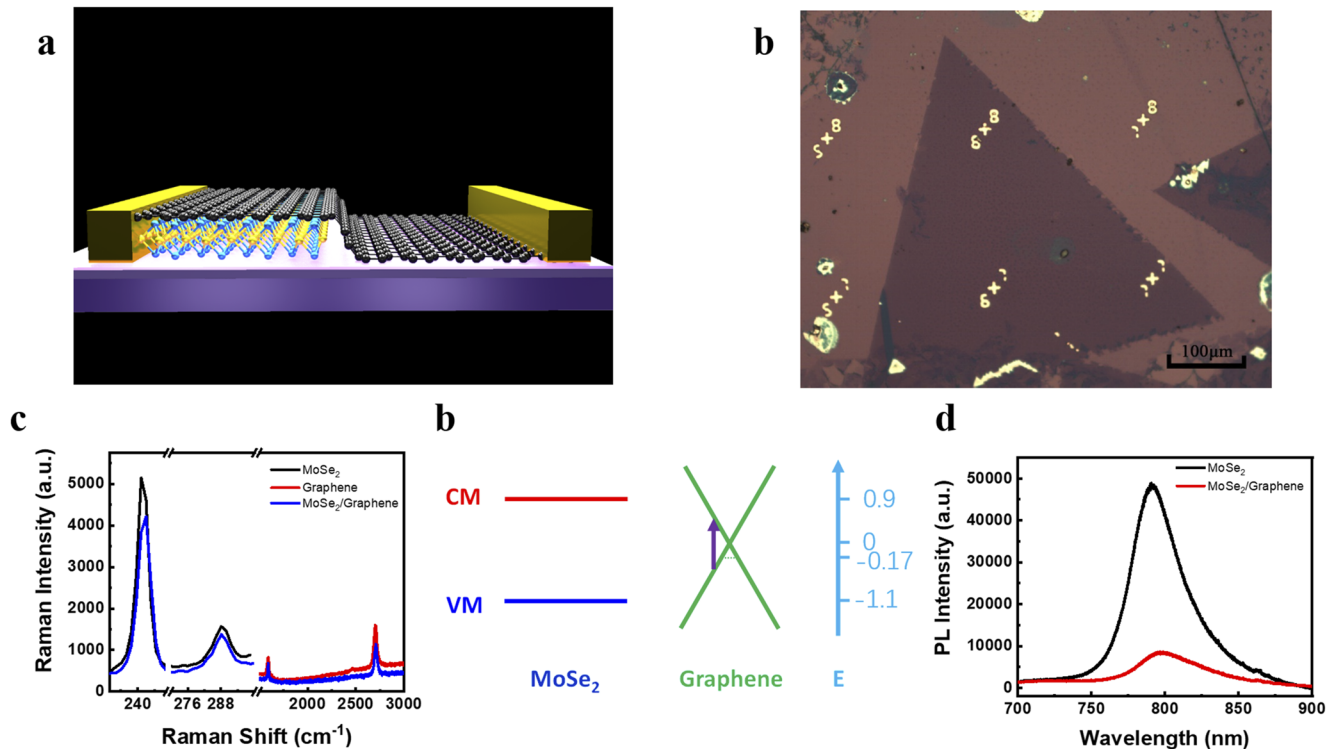
FIG. 1. Characterization of the graphene–$MoSe_2$ heterostructure. (a) Illustration of a two-atomic-layered optoelectronic device. (b) Optical image of the graphene–$MoSe_2$ heterostructure. The scale bar is 100 μm. (The dark triangle domain is $MoSe_2$ below a continuous monolayer of graphene. The top left corner is the graphene cracking area showing the lighter image of SiO_2. Location marks were prepared on the surface.) (c) Raman spectroscopy of graphene, $MoSe_2$, and graphene/$MoSe_2$ heterostructure. (d) Band alignment of the heterostructure. The energy levels of CBM (conduction band minimum of $MoSe_2$), the Dirac point, the Fermi level of graphene, and VBM (valence band maximum of $MoSe_2$) in eV are listed in the order from top to bottom on the right. The arrow indicates the electron excitation direction in graphene. (e) Photoluminescence (PL) spectra of the $MoSe_2$ monolayer and $MoSe_2$/graphene heterostructure.

MoSe$_2$/graphene heterostructure. The frequencies of vibrational modes A$_{1g}$ (242 cm^{-1}) and E$_{2g}^1$ (288 cm^{-1}) of the standalone MoSe$_2$ sample and the heterostructure match previously reported data of monolayer MoSe$_2$.[25] The characteristic 2D (2690 cm^{-1}) and G (1580 cm^{-1}) peaks of single-layered graphene are present in both the graphene–MoSe$_2$ heterostructure and the standalone graphene sample. The band arrangement of the graphene–MoSe$_2$ heterojunction is illustrated in Fig. 1(d). The bandgap of single-layer MoSe$_2$ is about 2.0 eV,[26,27] and the Dirac point of graphene is 0.9 eV lower than the bottom of the conduction band of single-layer MoSe$_2$. The Fermi level of graphene in the heterojunction is about −0.17 eV.

Charges/energy can efficiently transfer between MoSe$_2$ and graphene. As displayed in Fig. 1(e), the fluorescence spectrum peak of the heterojunction appears at 795 nm, the intensity (red line) of which is significantly reduced compared to that of the monolayer MoSe$_2$ (black line), indicating that the graphene layer enables efficient charges/energy transfer between the heterojunction layers, which causes fluorescence quenching.[28]

To enable optoelectronic measurements on the graphene/ MoSe$_2$ heterostructure, two gold electrodes are deposited onto the top of graphene at different locations, serving as the connectors to the external circuit. An optical image of the device is displayed in Fig. 2(a), where the circle electrodes are connected to the portion of standalone graphene, and the square electrodes are connected to the heterostructure. During the optoelectronic measurements, the drain/source direction is flipped as shown in Figs. 2(b) and 2(c).

All electrical measurements are performed at room temperature in ambient air. The photocurrent measurements are conducted with a semiconductor parameter analyzer and a probe station. The source–drain bias V$_{sd}$ = 0 and the gate voltage V$_g$ = 0 are used in all tests. The source–drain current–time (I$_{sd}$–t) curves directly reflect the photoelectric response of the heterojunction. In our first set of measurements, the source probe of the probe station is connected to the square electrode and the drain probe is connected to the circular electrode [Fig. 3(a)]. When a 405 nm laser irradiates on the heterostructure, a photocurrent is generated and detected [Fig. 3(c)]. Under 405 nm (~3.1 eV) excitation, the photons excite electrons in both graphene and MoSe$_2$ because the photonic energy is larger than the bandgap of MoSe$_2$ (2.0 eV) and graphene has a gapless

band structure. The photocurrent value is about −5.5 nA, indicating that the external current flows from the standalone portion of graphene to the portion on the top of MoSe$_2$. When the source and drain switches, the photocurrent value is positive [Fig. 3(d)]. Both results unambiguously demonstrate that the 405 nm photoexcitation generates extra electrons on the heterojunction portion of graphene compared to the standalone portion, indicating an overall electron flow from MoSe$_2$ to graphene inside the heterostructure upon photon excitation.

When a much lower photonic energy, 980 nm (1.3 eV), which is lower than the MoSe$_2$ bandgap (2.0 eV), is used to irradiate the heterostructure, the photons can only excite graphene but not MoSe$_2$. Surprisingly, a photocurrent also appears on the external circuit [Figs. 3(e) and 3(f)]. The current flow direction is the same as that excited with 405 nm, indicating that the photoexcitation generates an overall electron flow from MoSe$_2$ to graphene inside the heterostructure.

The results in Fig. 3 seem counterintuitive in three aspects: (1) should the device be short circuited, as both metal electrodes are attached to graphene that is a semi-metallic conductor? (2) According to the energy level in Fig. 1(c), the Fermi level of graphene is between the CB and VB of MoSe$_2$, which seems to require both electrons and holes to transfer to graphene and recombine there. (3) How can the excitation of electrons in graphene by 980 nm light produce extra electrons on itself?

B. Graphene's Fermi level shift in the heterostructure

The key to understand results in Fig. 3 and to answer the above questions is the charge separation on the graphene/MoSe$_2$ interface. The Fermi level of graphene is between the CBM and VBM of MeS$_2$. Dictated by the energy level alignment and driven by the requirement of minimizing the overall energy of the system, both electrons on the CBM and holes on the VBM of MeS$_2$ generated by photoexcitation should transfer to graphene and no charge separation should have occurred on the interface. However, this static point of view is correct only when the system reaches thermal equilibrium after long time relaxation. Before the dynamic process is considered, let us look into the Fermi level of graphene in the heterostructure.
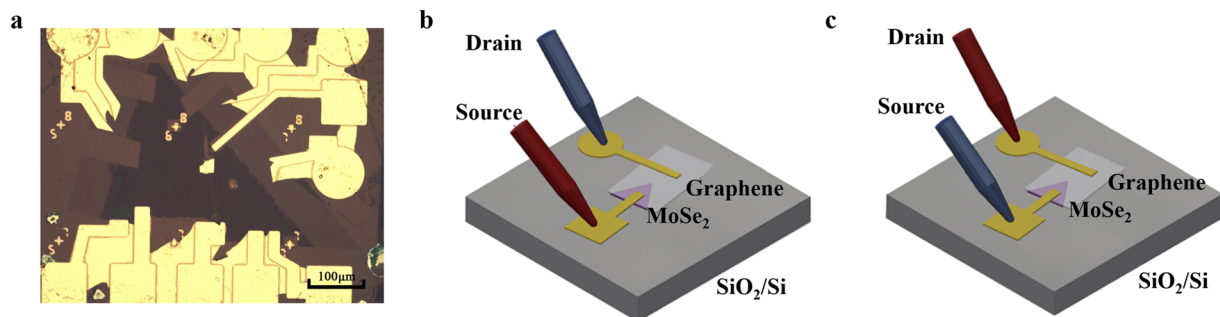

FIG. 2. Device and electrical measurement configuration of the graphene–MoSe$_2$ heterostructure. (a) Optical images of the graphene–MoSe$_2$ heterostructure device; the scale bar is 100 μm. (b) and (c) Schematic of the electrical measurement configurations.
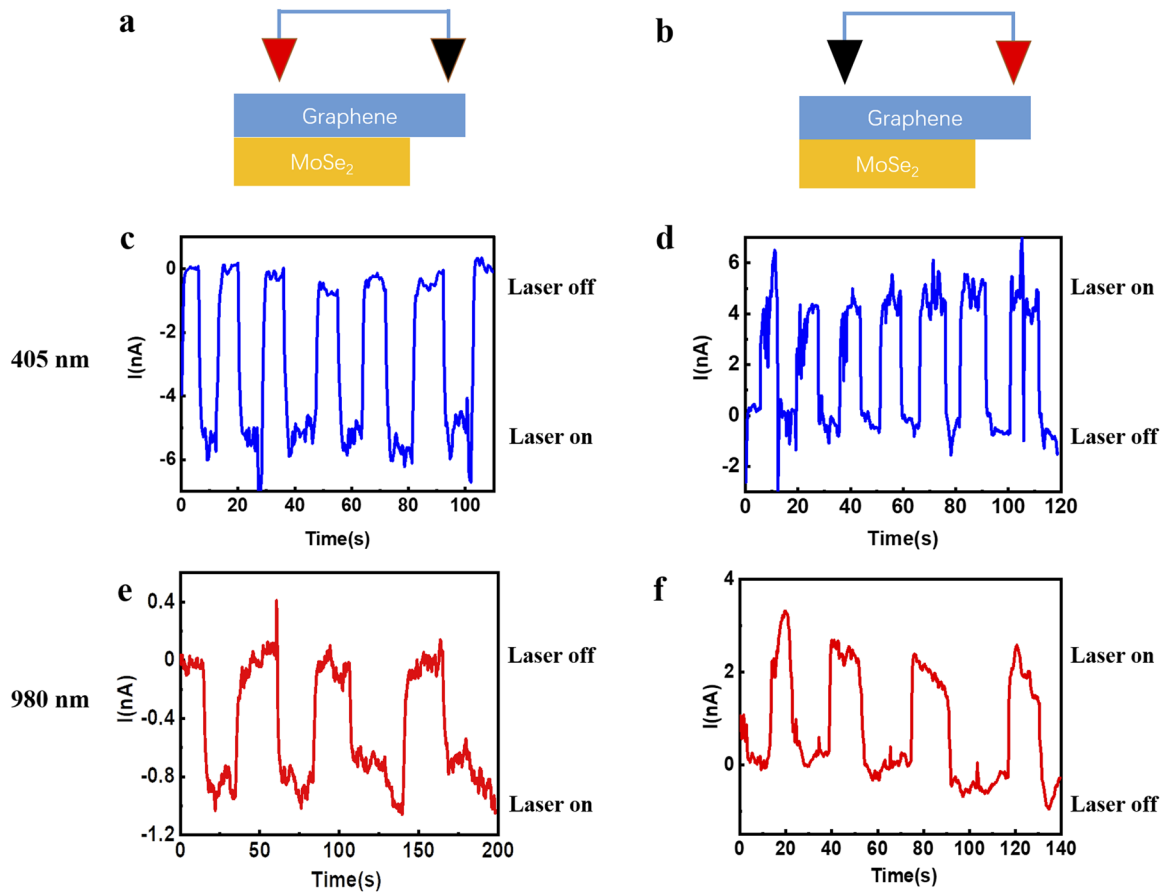
FIG. 3. Electrical measurements of the graphene–MoSe$_2$ heterostructure. (a) and (b) Measurement configurations: the drain/source direction is illustrated by the black and red triangles. (c) and (d) Photocurrent generation of the heterostructure at 405 nm. The photons excite both graphene and MoSe$_2$. (e) and (f) Photocurrent generation of the heterostructure at 980 nm. The photons only excite graphene but not MoSe$_2$.

Graphene used in this work is *p*-doped, and MoSe$_2$ is *n*-doped. Therefore, when a heterostructure is formed, electrons can transfer from MoSe$_2$ to graphene and lift the Fermi level of graphene. The detailed values of Fermi levels and numbers of electrons transferred can be obtained by analyzing ultrafast optical experimental results according to equations discussed below. The tight-binding Hamiltonian for the cone-like band structure of graphene is written as

$$H = \begin{bmatrix} 0, & \hbar v_{\mathrm{F}}(k_x + ik_y), \\ \hbar v_{\mathrm{F}}(k_x - ik_y), & 0, \end{bmatrix}, \quad (1)$$

where v_{F} is the Fermi velocity and k_x and k_y are the 2D components of the electronic wave vector **k**. With the Hamiltonian, the optical conductivity $[\sigma(\omega)]$ is written as the sum of the interband conductivity $[\sigma_{\mathrm{inter}}(\omega)]$ and the intraband conductivity $[\sigma_{\mathrm{intra}}(\omega)]$ given as follows:[23,29–31]

$$\sigma(\omega) = \sigma_{\mathrm{int\,er}}(\omega) + \sigma_{\mathrm{intra}}(\omega),$$

$$\sigma_{\mathrm{int\,er}}(\omega) = i\frac{e^2\hbar\omega}{\pi\hbar}\int_0^{+\infty} d\varepsilon \frac{1}{(2\varepsilon)^2 - (\hbar\omega + i\Gamma)^2}$$
$$\times [f_{\mathrm{FD}}(\varepsilon - \mu) - f_{\mathrm{FD}}(-\varepsilon - \mu)], \quad (2)$$

$$\sigma_{\mathrm{intra}}(\omega) = i\frac{e^2/\pi\hbar}{\hbar\omega + i\hbar/\tau_e}\int_0^{+\infty} d\varepsilon$$
$$\times [f_{\mathrm{FD}}(\varepsilon - \mu) + 1 - f_{\mathrm{FD}}(-\varepsilon - \mu)],$$

where f_{FD} is the Fermi–Dirac distribution function, μ is the chemical potential (Fermi energy), and e is the elementary charge. Γ is the broadening of the interband transitions, and τ_e is the relaxation time due to intraband carrier scattering. In the literature,[32,33] Γ lies between 0.01 and 0.06 eV, while τ_e is in the range of 5–40 fs. Here, considering that electronic motions typically occur within a few fs rather than tens of fs, we use the fast values $\Gamma = 0.062$ eV (500 cm^{-1}) and $\tau_e = 10$ fs throughout the study.

Applying the Fresnel equations, the change in optical transmission for s-polarized light due to the existence of graphene is given as

$$\frac{\Delta T_s}{T_0} \approx -\frac{2}{\cos\theta + n_{sub}\cos\theta''}\sqrt{\frac{\mu_0}{\varepsilon_0}}Re[\sigma(\omega)], \quad (3)$$

where θ is the incident angle; θ'' is the incident angle in the substrate; n_{sub} is the refractive index of the substrate; and ε_0 and μ_0 are the vacuum permittivity and permeability, respectively. The change in optical transmission for p-polarized light is

$$\frac{\Delta T_p}{T_0} \approx -\frac{2\cos\theta\cos\theta''}{n_{sub}\cos\theta + \cos\theta''}\sqrt{\frac{\mu_0}{\varepsilon_0}}Re[\sigma(\omega)]. \quad (4)$$

In our experiments, $\theta = 0°$, so we have

$$\frac{\Delta T}{T_0} \approx -\frac{2}{1 + n_{sub}}\sqrt{\frac{\mu_0}{\varepsilon_0}}Re[\sigma(\omega)], \quad (5)$$

where $n_{sub} = 1.39$ for the substrate CaF$_2$.

According to Eq. (5), by fitting the transient absorption spectra probed in the mid IR range and excited by 1.03 eV photons, the Fermi level of the standalone graphene is determined to be -0.19 eV and that of graphene in the graphene/MoSe$_2$ heterostructure is -0.17 (Fig. 4). The change is not significant, and the Fermi level in the heterostructure still lies between the CBM and VBM of MoSe$_2$.

The carrier density of graphene is

$$n = \int \frac{1}{(2\pi)^2}f(\varepsilon - \mu)d^2\mathbf{k} = \int \frac{k}{2\pi}f(\varepsilon - \mu)dk$$
$$= \int_0^{+\infty} \frac{\varepsilon}{2\pi(\hbar v_F)^2}f(\varepsilon - \mu)d\varepsilon. \quad (6)$$

When $|\mu| \gg k_B T$, Eq. (6) can be simplified into (degenerate spin and KK')

$$n \approx \frac{\mu^2}{\pi(\hbar v_F)^2}. \quad (7)$$

According to Eqs. (6) and (7), the Fermi level increase indicates that about $5\times10^{11}\frac{e}{cm^2}$ has transferred from MoSe$_2$ to graphene after they form a heterostructure.

C. Population redistribution in graphene after photoexcitation leading to charge transfers in the heterostructure

When electrons in graphene absorb photons, the energy they absorb can be rapidly converted into heat and change the electronic population distribution inside graphene, which leads to charge transfers on the heterostructure interface. In the following, the equations used to calculate the temperature inside graphene and the population change caused by the temperature change are discussed.

The interaction between phonons and electrons/holes in graphene is described by a deformation potential theory,[34,35] and the transition matrix element is determined to be

$$M_{\mathbf{k}',\mathbf{k}}^{(TO\,\&\,LO)} \approx 3\eta\sqrt{\frac{\hbar}{4M_C\omega_{phonon}}}, \quad (8)$$

where η is the electron–phonon coupling parameter and M_C is the mass of a carbon atom. The energy dispersion of the transverse optical (TO) and longitudinal optical (LO) phonon modes is ignored, and Eq. (8) accounts for the total contribution from TO and LO at Γ- or K-points. Both the emission and absorption of the phonons are considered under the second quantization. The probability of scattering from $\mathbf{k}$ to $\mathbf{k}'$ by strongly coupled optical phonons (SCOPs) is

$$W_{\mathbf{k}',\mathbf{k}}^{(TO\,\&\,LO)} = \frac{2\pi}{\hbar}\left|M_{\mathbf{k}',\mathbf{k}}^{(TO\,\&\,LO)}\right|^2\left[N_{\mathbf{q}}\delta(\varepsilon_{\mathbf{k}} - \varepsilon_{\mathbf{k}'} + \hbar\omega_{phonon})\right.$$
$$\left. + (N_{\mathbf{q}} + 1)\delta(\varepsilon_{\mathbf{k}} - \varepsilon_{\mathbf{k}'} - \hbar\omega_{phonon})\right]$$
$$= \frac{9\pi\eta^2}{2M_C\omega_{phonon}}\left[N_{\mathbf{q}}\delta(\varepsilon_{\mathbf{k}} - \varepsilon_{\mathbf{k}'} + \hbar\omega_{phonon})\right.$$
$$\left. + (N_{\mathbf{q}} + 1)\delta(\varepsilon_{\mathbf{k}} - \varepsilon_{\mathbf{k}'} - \hbar\omega_{phonon})\right], \quad (9)$$

where $N_{\mathbf{q}}$ is the phonon occupation number described by the Bose–Einstein distribution. The first and second terms in the square
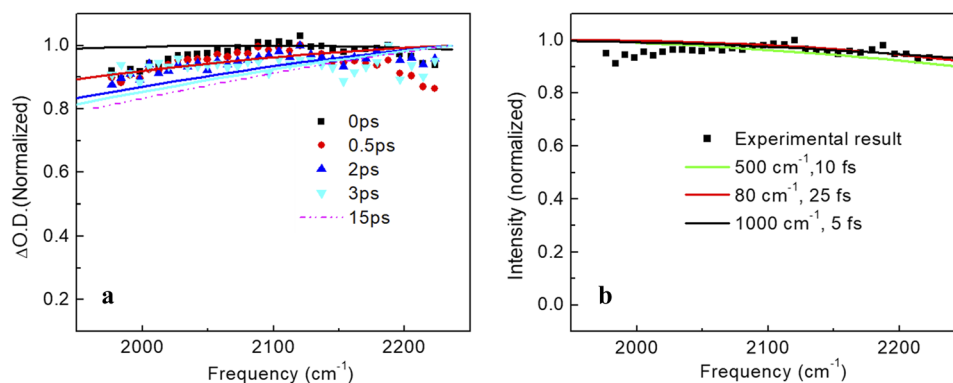

FIG. 4. (a) Standalone graphene and (b) graphene in the graphene/MoSe$_2$ heterostructure transient absorption spectra probed in the IR region excited by 1.03 eV photons. Dots indicate experimental data, and lines indicate calculations. Calculation parameters for (a) are the graphene Fermi level $\mu = -0.19$ eV, phonon fraction $f_{SCOPs} = 0.15$, photon flux absorbed F = 0.0069 J/m^2, pump/probe response time t = 170 fs, the dephasing time of 10 fs, and electron–phonon coupling parameter $\eta = 6.0\frac{eV}{Å}$. For (b) (the delay time is 0 ps), $\mu = -0.17$ eV, phonon fraction $f_{SCOPs} = 0.15$, photon flux absorbed F = 0.0046 J/m^2, response time t = 170 fs, and electron–phonon coupling parameter $\eta = 6.0\frac{eV}{Å}$.

brackets correspond to the emission and absorption processes, respectively. Integrating $\mathbf{k}'$ gives the scattering rate of $\mathbf{k}$ as

$$
\begin{aligned}
R_{\mathbf{k} \to *} &= \int W_{\mathbf{k}',\mathbf{k}}^{(\text{TO \& LO})} \frac{A}{(2\pi)^2} d^2\mathbf{k}' \\
&= \frac{9\eta^2}{2\hbar^2 \rho v_F^2 \omega_{\text{phonon}}} \left[(\varepsilon_{\mathbf{k}} + \hbar\omega_{\text{phonon}})N_{\mathbf{q}} + (\varepsilon_{\mathbf{k}} - \hbar\omega_{\text{phonon}}) \right. \\
&\quad \left. \times (N_{\mathbf{q}} + 1) \right],
\end{aligned}
\tag{10}
$$

where ρ is the 2D mass density of graphene. Therefore, the rate of phonon emission per unit area is

$$
\begin{aligned}
\frac{dN_{\text{emission}}}{dt} &= \int \frac{9\eta^2}{2\hbar^2 \rho v_F^2 \omega_{\text{phonon}}} (\varepsilon_{\mathbf{k}} - \hbar\omega_{\text{phonon}}) \\
&\quad \times (N_{\mathbf{q}} + 1) f_{\text{FD}}(\varepsilon_{\mathbf{k}}) \left(1 - f_{\text{FD}}(\varepsilon_{\mathbf{k}} - \hbar\omega_{\text{phonon}})\right) \\
&\quad \times \frac{1}{(2\pi)^2} d^2\mathbf{k} = \frac{9\eta^2}{4\pi(\hbar v_F)^4 \rho\omega_{\text{phonon}}} (N_{\mathbf{q}} + 1) \\
&\quad \times \int \varepsilon_{\mathbf{k}} (\varepsilon_{\mathbf{k}} - \hbar\omega_{\text{phonon}}) f_{\text{FD}}(\varepsilon_{\mathbf{k}}) \\
&\quad \times \left(1 - f_{\text{FD}}(\varepsilon_{\mathbf{k}} - \hbar\omega_{\text{phonon}})\right) d\varepsilon_{\mathbf{k}},
\end{aligned}
\tag{11}
$$

and the rate of phonon absorption is

$$
\begin{aligned}
\frac{dN_{\text{adsorption}}}{dt} &= \frac{9\eta^2}{4\pi(\hbar v_F)^4 \rho\omega_{\text{phonon}}} N_{\mathbf{q}} \\
&\quad \times \int \varepsilon_{\mathbf{k}} (\varepsilon_{\mathbf{k}} + \hbar\omega_{\text{phonon}}) f_{\text{FD}}(\varepsilon_{\mathbf{k}}) \\
&\quad \times \left(1 - f_{\text{FD}}(\varepsilon_{\mathbf{k}} + \hbar\omega_{\text{phonon}})\right) d\varepsilon_{\mathbf{k}},
\end{aligned}
\tag{12}
$$

which are used to simulate the heat transfer between electrons/holes and SCOPs. Strongly coupled optical phonons (SCOPs) are in-plane optical phonons for which intra- and inter-valley carrier scattering can simultaneously conserve energy and momentum.[36] The considered SCOPs include phonons near the Γ-point with energy ~200 meV (for intra-valley carrier scattering) and those near the K-point with energy ~150 meV (for inter-valley carrier scattering).

The heat capacity of SCOPs is described by the Einstein model, and the fraction of the Brillouin zone filled by the SCOPs, f_{SCOPs}, for simplicity, is assumed to be temperature independent.[23] The energy stored in the SCOP subsystem relaxes at a rate of $1/\tau_{\text{ph}}$ to lower energy phonons.[23,37]

At temperature T, the population of electrons in graphene that have higher energy than the CBM value of MoSe$_2$, capable of interlayer transferring, is calculated as

$$
n_e(T; E_{\text{CBM}}) = \int_{E_{\text{CBM}}}^{+\infty} \frac{\varepsilon}{2\pi(\hbar v_F)^2} f(\varepsilon - \mu) d\varepsilon.
\tag{13}
$$

Similarly, the population of holes capable of interlayer transferring is

$$
n_h(T; E_{\text{VBM}}) = \int_{-\infty}^{E_{\text{VBM}}} \frac{\varepsilon}{2\pi(\hbar v_F)^2} f(-\varepsilon + \mu) d\varepsilon.
\tag{14}
$$

According to the above equations, the temperature of graphene in the heterostructure after 1.03 eV *excitation* is calculated and displayed in Fig. 5(a). The temperature can jump as high as nearly 1400 K and then rapidly drop to about 300 K within 5 ps. By subtracting the *populations* before excitation (T_0 = 300 K), the ratio of n_h/n_e calculated is plotted in Fig. 5(b). With 100% flux of 1.03 eV excitation, the electronic temperature is as high as 1583 K and n_h/n_e is 4.9. With 2/3 flux, the electronic temperature is 1399 K and n_h/n_e is 5.8. Charge transfers result in a lower temperature, so the exact experimental n_h/n_e lies between these two values. Interlayer charge transfers and electronic thermalization in graphene are fast (<50 fs).[23,28,38] Thus, they can be treated as semi-instantaneous compared to the graphene electron/hole recombination (100–200 fs) and the interlayer exciton formation (~500 fs). Therefore, the transfer of photo-excited carriers between two layers forms a quasi-equilibrium. The electron/hole population ratio in MoSe$_2$ is approximately equal to that in graphene. Once carriers form interlayer excitons, the quasi-equilibrium is perturbed and more carriers are transferred to MoSe$_2$ as the charge carriers in graphene continuously adjust their population distributions. This process results in a substantial total number of transferred holes even though the hole population in graphene below the VBM of MoSe$_2$ is only a small portion of the total number photo-generated. The process results in that the majority of interlayer excitons have their holes in the MoSe$_2$ layer and electrons in graphene. The estimated exciton density is about 0.45×10^{12} and 0.58×10^{12} cm^{-2} under our experimental excitation photon energy of 1.03 and 3.1 eV, respectively. Another possible (but minor) mechanism can also lead to that electrons stay in graphene and holes prefer MoSe$_2$. According to the literature,[39] charged impurities in MoSe$_2$ and graphene can produce an effective electric field that is from graphene to MoSe$_2$. Such an
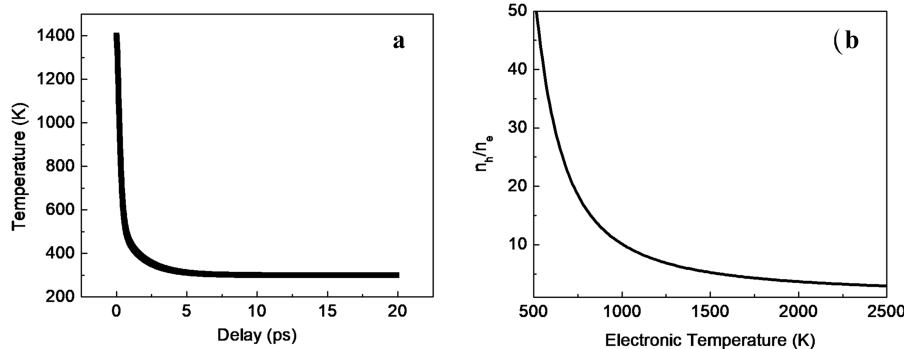

FIG. 5. (a) Calculated temperature of graphene in the heterostructure after 1.03 eV excitation. Calculation parameters: graphene Fermi level $\mu = -0.17$ eV, phonon fraction $f_{\text{SCOPs}} = 0.15$, photon flux absorbed $F = 0.0046$ J/m^2, pump response time $t = 170$ fs, and electron–phonon coupling parameter $\eta = 6.0 \frac{\text{eV}}{\text{Å}}$. (b) Temperature dependent n_h/n_e.
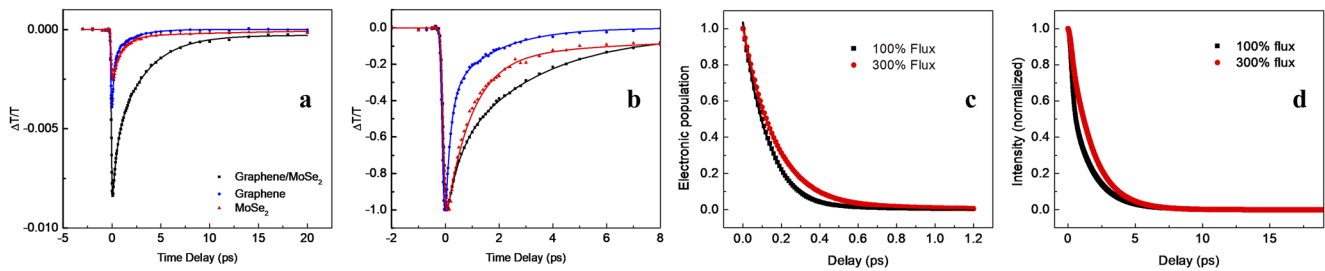
FIG. 6. (a) and (b) Unnormalized and normalized waiting time-dependent transient IR signals detected at 2185 cm^{-1} of the MoSe$_2$/graphene heterostructure, MoSe$_2$, and graphene excited with 3.1 eV (400 nm) photons. (c) and (d) Calculated graphene 400 nm-excitation/2185 cm^{-1}-detection electronic dynamics and signals with two different excitation fluxes. Calculation parameters: graphene Fermi level $\mu = -0.17$ eV, phonon fraction $f_{SCOPs} = 0.15$, photon flux absorbed $F = 0.0087 \frac{J}{m^2}$ (100% flux) and $0.0261 \frac{J}{m^2}$, pump response time $t = 170$ fs, and electron–phonon coupling parameter $\eta = 6.0 \frac{eV}{\text{Å}}$. The electronic decay time is 130 fs with 100% and 170 fs with 300% flux.

electric field can provide driving force for holes to move to MoSe$_2$ and for electrons to go to graphene.

As discussed above, the photoexcitation naturally leads to electrons flowing into graphene from MeS$_2$. The electronic density in graphene, therefore, is higher in the portion stacked with MoSe$_2$ than in the stand alone portion. Electrons can diffuse through the entire graphene or flow through the external circuit to reach equilibrium. Since the conductivity of the external circuit is larger than the single layer graphene, it is reasonable to observe photocurrent in the external circuit as displayed in Fig. 3, and the observed current direction is consistent with the analysis.

D. More absorption resulting in slower dynamics

The above analyses can also well explain slower dynamics in the heterostructure than in graphene or MoSe$_2$ [Figs. 6(a) and 6(b)] excited with 3.1 eV photons (similar results with the excitation of other photonic energy). Single layer MoSe$_2$ absorbs 14% and graphene absorbs 4.14% of 3.1 eV photons. Because the Fermi level of graphene lies between the CBM and VBM of MoSe$_2$ and if ideal fast equilibrium is assumed, ~9% of excitation photons (a total of 18%) would be in either layer of the heterostructure, which means that at least more than 33% of the electrons excited in MoSe$_2$ move to graphene where the energy is converted into thermal energy. The charge transfers result in a higher electronic temperature in graphene. According to calculations [Figs. 6(c) and 6(d)] based on the above equations, electronic dynamics and optical signal decay are slower with a larger excitation flux (or a higher temperature).

III. CONCLUDING REMARKS

In summary, an optoelectronic device composed of only two atomic layers (one layer of graphene and one layer of semiconductor) is demonstrated to be feasible. The key for such a device to function is to utilize the fast electronic relaxation and thermalization of photoexcitation in graphene, which leads to population redistribution and charge transfers on the interface. The overall result is that more electrons accumulated on the portion of graphene stacked with the semiconductor than the stand alone portion, which can produce a current through the external circuit. The principle demonstrated in this work is expected to be general on the interfaces of graphene with other materials.

A. Experiments
1. MoSe$_2$ monolayer growth

The CVD method was used to grow MoSe$_2$.[12] The Se and Mo precursors, selenium pellets, and MoO$_3$ were placed into the same alumina boat. A clean Si wafer with a 300 nm thin layer of SiO$_2$ was placed face down in the boat, which was located at the center of the tube furnace. The furnace temperature was raised up to 750 °C with a heating rate of 50 °C/min and then held at 750 °C for 20 min, yielding MoSe$_2$ triangle domains, and finally cooled down to room temperature. 50 sccm 15% H$_2$/Ar was used as a carrier gas and reducing atmosphere during the deposition process. The growth was carried on under atmospheric pressure. The output curves and transfer curves of the n-doped MoSe$_2$ used in the experiments are illustrated (Fig. 7).
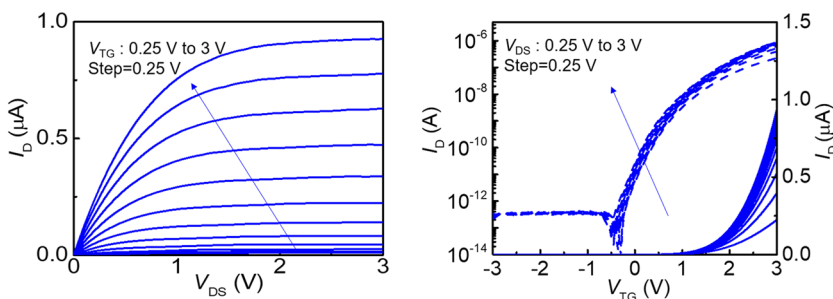

FIG. 7. Output curves and transfer curves of the n-doped MoSe$_2$ used in the experiments.

2. Graphene monolayer growth

The CVD method was used to grow graphene on an electropolished copper foil with methane as a precursor. The copper foil was annealed at 1000 °C for 20 min, followed by graphene growth for 9 min using 3.5 sccm of methane at the same temperature. 15% H_2/Ar was used as a carrier gas, and the pressure was kept around 1 Torr during the whole process.

3. Heterostructure preparation

$MoSe_2$ was transferred onto the CaF_2 substrates for transmission mode laser experiments. A thin layer of PMMA was spin-coated onto the sample at a speed of 4000 rpm. The sample is carefully placed to float in a buffer HF (1:5). After 20 h corrosion, PMMA can be fished with a glass plate and then moved to Di-water for rinsing. The pre-cleaned CaF_2 windows were used to fish the PMMA sheets, and samples stayed at room temperature and in vacuum for 24 h. Finally, acetone is used to remove PMMA. Graphene on the Cu foils spin-coated with PMMA is dissolved in Cu_2Fe_3. The graphene PMMA sheet is fished and transferred onto the $MoSe_2$ monolayers. PMMA is removed with acetone, and the sample is annealed in vacuum at 300 °C for 3 h.

4. Raman and photoluminescence measurements

Raman spectroscopy and PL spectroscopy were carried out using a Horiba Jobin Yvon LabRAM HR-Evolution Raman microscope. The excitation light is a 532 nm laser, with an estimated laser spot size of 1 μm and a laser power of 1 mW.

5. Device preparation and electrical measurements

Photoresist is spin-coated on the heterojunction at a rotation speed of 4000 r/min and a duration of 30 s. The photoresist is dried at 110 °C for 3 min and then exposed to a photolithography machine to define the location marks. Chromium (80 Å) and gold (600 Å) were deposited by thermal evaporation, and the deposition rate is controlled at every 30 s/Å. Under the microscope, the device pattern was selected and designed according to the location mark. After the PMMA was spin-coated onto the sample, EBL was performed according to the designed pattern. The sample was soaked in the developer (methyl isobutyl ketone:isopropanol = 3:1) and fixing solution (isopropanol) for 30 and 15 s, respectively. Then, the sample was placed into the plasma treatment equipment. The graphene and $MoSe_2$ uncovered by PMMA were etched by oxygen plasma, and acetone was used to remove the remaining PMMA. The second round of EBL and thermal evaporation was performed to construct electrodes as the same method above. The photocurrent measurements were conducted with a semiconductor parameter analyzer (Agilent 4155C) and a probe station. The source/drain bias V_{sd} = 0 and the gate voltage Vg = 0 in all tests.

6. Ultrafast visible-NIR/infrared microspectroscopy

The femtosecond amplifier laser system is used at a repetition rate of 1 kHz, an energy of 1.6 mJ per pulse, a central wavelength of 800 nm, and a pulse duration of ~40 fs. The output is split into two parts to generate pump pulses at visible and near-IR-1 and the probe pulses in the whole mid-IR region or near-IR-2.[40,41] The interaction spot on the samples varied from 120 to 250 micron, and the probe light was focused at the sample by the reflective objective lens (15X/0.28NA, Edmund Optics Inc.) to reduce the

spot size to the level of the sample area (<40 μm). A microscope digital camera is used to align the pump/probe beam to a proper sample area. The probe light is detected using a liquid-nitrogen-cooled mercury–cadmium–telluride (MCT) array detector or an InSb detector. The time delay between the pump light and probe light is controlled by a motorized delay stage.

AUTHOR DECLARATIONS

Conflict of Interest

The authors declare no conflict of interest.

DATA AVAILABILITY

The data that support the findings of this study are available from the corresponding author upon reasonable request.

REFERENCES

[1] J. Shim, H.-Y. Park, D.-H. Kang, J.-O. Kim, S.-H. Jo, Y. Park, and J.-H. Park, "Electronic and optoelectronic devices based on two-dimensional materials: From fabrication to application," Adv. Electron. Mater. **3**(4), 1600364 (2017).

[2] K. S. Novoselov, A. Mishchenko, A. Carvalho, and A. H. Castro Neto, "2D materials and van der Waals heterostructures," Science **353**(6298), aac9439 (2016).

[3] K. F. Mak and J. Shan, "Photonics and optoelectronics of 2D semiconductor transition metal dichalcogenides," Nat. Photonics **10**(4), 216–226 (2016).

[4] A. G. Ricciardulli and P. W. M. Blom, "Solution-processable 2D materials applied in light-emitting diodes and solar cells," Adv. Mater. Technol. **5**(8), 1900972 (2020).

[5] Z. Yin, S. Sun, T. Salim, S. Wu, X. Huang, Q. He, Y. M. Lam, and H. Zhang, "Organic photovoltaic devices using highly flexible reduced graphene oxide films as transparent electrodes," ACS Nano **4**(9), 5263–5268 (2010).

[6] A. G. Ricciardulli, S. Yang, X. Feng, and P. W. M. Blom, "Solution-processable high-quality graphene for organic solar cells," ACS Appl. Mater. Interfaces **9**(30), 25412–25417 (2017).

[7] D. Konios, C. Petridis, G. Kakavelakis, M. Sygletou, K. Savva, E. Stratakis, and E. Kymakis, "Reduced graphene oxide micromesh electrodes for large area, flexible, organic photovoltaic devices," Adv. Funct. Mater. **25**(15), 2213–2221 (2015).

[8] S.-S. Li, K.-H. Tu, C.-C. Lin, C.-W. Chen, and M. Chhowalla, "Solution-processable graphene oxide as an efficient hole transport layer in polymer solar cells," ACS Nano **4**(6), 3169–3174 (2010).

[9] J. Liu, Y. Xue, and L. Dai, "Sulfated graphene oxide as a hole-extraction layer in high-performance polymer solar cells," J. Phys. Chem. Lett. **3**(14), 1928–1933 (2012).

[10] Y. Lin, B. Adilbekova, Y. Firdaus, E. Yengel, H. Faber, M. Sajjad, X. Zheng, E. Yarali, A. Seitkhan, and O. M. Bakr, "17% efficient organic solar cells based on liquid exfoliated WS_2 as a replacement for PEDOT:PSS," Adv. Mater. **31**(46), 1902965 (2019).

[11] D. Geng, X. Zhao, Z. Chen, W. Sun, W. Fu, J. Chen, W. Liu, W. Zhou, and K. P. Loh, "Direct synthesis of large-area 2D Mo_2C on in situ grown graphene," Adv. Mater. **29**(35), 1700072 (2017).

[12] X. Wang, Y. Gong, G. Shi, W. L. Chow, K. Keyshar, G. Ye, R. Vajtai, J. Lou, Z. Liu, and E. Ringe, "Chemical vapor deposition growth of crystalline monolayer $MoSe_2$," ACS Nano **8**(5), 5125–5131 (2014).

[13] K. S. Novoselov, D. Jiang, F. Schedin, T. J. Booth, V. V. Khotkevich, S. V. Morozov, and A. K. Geim, "Two-dimensional atomic crystals," Proc. Natl. Acad. Sci. U. S. A. **102**(30), 10451–10453 (2005).

[14] K. S. Novoselov, A. K. Geim, S. V. Morozov, D. Jiang, Y. Zhang, S. V. Dubonos, I. V. Grigorieva, and A. A. Firsov, "Electric field effect in atomically thin carbon films," Science **306**(5696), 666–669 (2004).

[15] A. H. Castro Neto, F. Guinea, N. M. R. Peres, K. S. Novoselov, and A. K. Geim, "The electronic properties of graphene," Rev. Mod. Phys. **81**(1), 109 (2009).

[16] F. Schwierz, "Graphene transistors," Nat. Nanotechnol. **5**(7), 487–496 (2010).

[17] A. K. Geim and I. V. Grigorieva, "Van der Waals heterostructures," Nature **499**(7459), 419–425 (2013).

[18] L. Britnell, R. V. Gorbachev, R. Jalil, B. D. Belle, F. Schedin, A. Mishchenko, T. Georgiou, M. I. Katsnelson, L. Eaves, and S. V. Morozov, "Field-effect tunneling transistor based on vertical graphene heterostructures," Science **335**(6071), 947–950 (2012).

[19] Q. H. Wang, K. Kalantar-Zadeh, A. Kis, J. N. Coleman, and M. S. Strano, "Electronics and optoelectronics of two-dimensional transition metal dichalcogenides," Nat. Nanotechnol. **7**(11), 699–712 (2012).

[20] S. J. Haigh, A. Gholinia, R. Jalil, S. Romani, L. Britnell, D. C. Elias, K. S. Novoselov, L. A. Ponomarenko, A. K. Geim, and R. Gorbachev, "Cross-sectional imaging of individual layers and buried interfaces of graphene-based heterostructures and superlattices," Nat. Mater. **11**(9), 764–767 (2012).

[21] K. Roy, M. Padmanabhan, S. Goswami, T. P. Sai, G. Ramalingam, S. Raghavan, and A. Ghosh, "Graphene–MoS$_2$ hybrid structures for multifunctional photoresponsive memory devices," Nat. Nanotechnol. **8**(11), 826–830 (2013).

[22] Y. Zhang, T.-R. Chang, B. Zhou, Y.-T. Cui, H. Yan, Z. Liu, F. Schmitt, J. Lee, R. Moore, and Y. Chen, "Direct observation of the transition from indirect to direct bandgap in atomically thin epitaxial MoSe$_2$," Nat. Nanotechnol. **9**(2), 111 (2014).

[23] L. M. Malard, K. Fai Mak, A. H. Castro Neto, N. M. R. Peres, and T. F. Heinz, "Observation of intra- and inter-band transitions in the transient optical response of graphene," New J. Phys. **15**(1), 015009 (2013).

[24] H. C. Lee, W.-W. Liu, S.-P. Chai, A. R. Mohamed, A. Aziz, C.-S. Khe, N. M. S. Hidayah, and U. Hashim, "Review of the synthesis, transfer, characterization and growth mechanisms of single and multilayer graphene," RSC Adv. **7**(26), 15644–15693 (2017).

[25] P. Tonndorf, R. Schmidt, P. Böttger, X. Zhang, J. Börner, A. Liebig, M. Albrecht, C. Kloc, O. Gordan, and D. R. T. Zahn, "Photoluminescence emission and Raman response of monolayer MoS$_2$, MoSe$_2$, and WSe$_2$," Opt. Express **21**(4), 4908–4916 (2013).

[26] T. C. Berkelbach, M. S. Hybertsen, and D. R. Reichman, "Theory of neutral and charged excitons in monolayer transition metal dichalcogenides," Phys. Rev. B **88**(4), 045318 (2013).

[27] M. M. Ugeda, A. J. Bradley, S.-F. Shi, F. H. da Jornada, Y. Zhang, D. Y. Qiu, W. Ruan, S.-K. Mo, Z. Hussain, and Z.-X. Shen, "Giant bandgap renormalization and excitonic effects in a monolayer transition metal dichalcogenide semiconductor," Nat. Mater. **13**(12), 1091–1095 (2014).

[28] X. Hong, J. Kim, S.-F. Shi, Y. Zhang, C. Jin, Y. Sun, S. Tongay, J. Wu, Y. Zhang, and F. Wang, "Ultrafast charge transfer in atomically thin MoS$_2$/WS$_2$ heterostructures," Nat. Nanotechnol. **9**(9), 682–686 (2014).

[29] J. M. Dawlaty, S. Shivaraman, J. Strait, P. George, M. Chandrashekhar, F. Rana, M. G. Spencer, D. Veksler, and Y. Chen, "Measurement of the optical absorption spectra of epitaxial graphene from terahertz to visible," Appl. Phys. Lett. **93**(13), 131905 (2008).

[30] V. P. Gusynin, S. G. Sharapov, and J. P. Carbotte, "Unusual microwave response of Dirac quasiparticles in graphene," Phys. Rev. Lett. **96**(25), 256802 (2006).

[31] S. A. Mikhailov and K. Ziegler, "New electromagnetic mode in graphene," Phys. Rev. Lett. **99**(1), 016803 (2007).

[32] Q. Ma, T. I. Andersen, N. L. Nair, N. M. Gabor, M. Massicotte, C. H. Lui, A. F. Young, W. Fang, K. Watanabe, T. Taniguchi, J. Kong, N. Gedik, F. H. L. Koppens, and P. Jarillo-Herrero, "Tuning ultrafast electron thermalization pathways in a van der Waals heterostructure," Nat. Phys. **12**(5), 455–459 (2016).

[33] T. Kampfrath, L. Perfetti, F. Schapper, C. Frischkorn, and M. Wolf, "Strongly coupled optical phonons in the ultrafast dynamics of the electronic energy and current relaxation in graphite," Phys. Rev. Lett. **95**(18), 187403 (2005).

[34] Z. Z. Li, J. Y. Wang, and Z. R. Liu, "Intrinsic carrier mobility of Dirac cones: The limitations of deformation potential theory," J. Chem. Phys. **141**(14), 144107 (2014).

[35] C.-H. Park, N. Bonini, T. Sohier, G. Samsonidze, B. Kozinsky, M. Calandra, F. Mauri, and N. Marzari, "Electron-phonon interactions and the intrinsic electrical resistivity of graphene," Nano Lett. **14**(3), 1113–1119 (2014).

[36] S. Piscanec, M. Lazzeri, F. Mauri, A. C. Ferrari, and J. Robertson, "Kohn anomalies and electron-phonon interactions in graphite," Phys. Rev. Lett. **93**(18), 185503 (2004).

[37] C. H. Lui, K. F. Mak, J. Shan, and T. F. Heinz, "Ultrafast photoluminescence from graphene," Phys. Rev. Lett. **105**(12), 127404 (2010).

[38] H. Chen, X. Wen, J. Zhang, T. Wu, Y. Gong, X. Zhang, J. Yuan, C. Yi, J. Lou, P. M. Ajayan, W. Zhuang, G. Zhang, and J. Zheng, "Ultrafast formation of interlayer hot excitons in atomically thin MoS$_2$/WS$_2$ heterostructures," Nat. Commun. **7**, 12512 (2016).

[39] W. J. Zhang, C. P. Chuu, J. K. Huang, C. H. Chen, M. L. Tsai, Y. H. Chang, C. T. Liang, Y. Z. Chen, Y. L. Chueh, J. H. He, M. Y. Chou, and L. J. Li, "Ultrahigh-gain photodetectors based on atomically thin graphene-MoS$_2$ heterostructures," Sci. Rep. **4**, 3826 (2014).

[40] H. Chen, H. Bian, J. Li, X. Guo, X. Wen, and J. Zheng, "Molecular conformations of crystalline L-cysteine determined with vibrational cross angle measurements," J. Phys. Chem. B **117**(49), 15614–15624 (2013).

[41] H. Chen, Y. Zhang, J. Li, H. Liu, D.-E. Jiang, and J. Zheng, "Vibrational cross-angles in condensed molecules: A structural tool," J. Phys. Chem. A **117**(35), 8407–8415 (2013).